difference in the resulting $\partial\theta/\partial z$ is 0.2×10^{-4} °C m^{-1}. Taking this as the uncertainty in $\partial\theta/\partial z$, together with the uncertainty caused by the relatively small number of stations, we allocate an uncertainty of 0.3×10^{-4} °C m^{-1}. The vertical salinity gradient at this isopycnal was 6.8×10^{-6} m^{-1} with an estimated uncertainty of 0.5×10^{-6} m^{-1}.

Geothermal heating

In some regions of the sea floor, geothermal heating is negligible. Flow through the oceanic crust is a function of the age of the crust; younger crust provides greater heating. The Scotia Sea exhibits a wide variety of ages. We estimate a typical value for G to be 0.1 W m^{-2}, and use this in the heat budget equation with an uncertainty of 0.1 W m^{-2}.

Seawater density, specific heat capacity

For the situation where geothermal heating is included, values for the *in situ* density of sea water and the specific heat capacity are required. We used the HASO climatological data set to determine representative median values. The uncertainty in these is negligible compared with other uncertainties in the calculation.

Received 9 October; accepted 19 December 2001.

1. Munk, W. H. Abyssal recipes. *Deep-Sea Res.* **13,** 207–230 (1966).
2. Munk, W. H. & Wunsch, C. Abyssal recipes II: energetics of tidal and wind mixing. *Deep-Sea Res. I* **45,** 1997–2010 (1998).
3. Toole, J. M. & McDougall, T. J. in *Ocean Circulation and Climate* (eds Siedler, G., Church, J. & Gould, J.) 337–355 (Academic, London, 2001).
4. Toole, J. M., Polzin, K. L. & Schmitt, R. W. Estimates of diapycnal mixing in the abyssal ocean. *Science* **264,** 1120–1123 (1994).
5. Whitehead, J. A. & Worthington, L. V. The flux and mixing rates of Antarctic Bottom Water within the North Atlantic. *J. Geophys. Res.* **87,** 7903–7924 (1982).
6. Hogg, N. G., Biscaye, P., Gardner, W. & Schmitz, W. J. On the transport and modification of Antarctic Bottom water in the Vema Channel. *J. Mar. Res.* **40** (suppl.), 231–263 (1982).
7. Saunders, P. M. Flow through Discovery gap. *J. Phys. Oceanogr.* **17,** 631–643 (1987).
8. Barton, E. D. & Hill, A. E. Abyssal flow through the Amirante Trench (Western Indian Ocean). *Deep-Sea Res. A* **36,** 1121–1126 (1989).
9. Durrieu de Madron, X. & Weatherly, G. Circulation, transport and bottom boundary layers of the deep currents in the Brazil Basin. *J. Mar. Res.* **52,** 583–638 (1994).
10. Roemmich, D., Huatala, S. & Rudnick, D. Northward abyssal transport through the Samoan Passage and adjacent regions. *J. Geophys. Res.* **101,** 14039–14055 (1996).
11. McCarthy, M. C., Talley, L. D. & Baringer, M. O. Deep upwelling and diffusivity in the southern Central Indian Basin. *Geophys. Res. Lett.* **24,** 2801–2804 (1997).
12. Morris, M. Y., Hall, M. M., St Laurent, L. C. & Hogg, N. G. Abyssal mixing in the Brazil Basin. *J. Phys. Oceanogr.* **31,** 3331–3348 (2001).
13. Polzin, K. L., Speer, K. G., Toole, J. M. & Schmitt, R. W. Intense mixing of Antarctic Bottom Water in the equatorial Atlantic Ocean. *Nature* **380,** 54–57 (1996).
14. Polzin, K. L., Toole, J. M., Ledwell, J. R. & Schmitt, R. W. Spatial variability of turbulent mixing in the abyssal ocean. *Science* **276,** 93–96 (1997).
15. Ledwell, J. R. *et al.* Evidence for enhanced mixing over rough topography in the abyssal ocean. *Nature* **403,** 179–182 (2000).
16. Smith, W. H. F. & Sandwell, D. T. Global sea floor topography from satellite altimetry nd ship depth soundings. *Science* **277,** 1956–1962 (1997).
17. Huang, R. X. Mixing and energetics of the oceanic thermohaline circulation. *J. Phys. Oceanogr.* **29,** 727–746 (1999).
18. Zhang, J., Schmitt, R. W. & Huang, R. X. The relative influence of diapycnal mixing and hydrologic forcing on the stability of the thermohaline circulation. *J. Phys. Oceanogr.* **29,** 1096–1108 (1999).
19. Ganachaud, A. & Wunsch, C. Improved estimates of global ocean circulation, heat transport and mixing from hydrographic data. *Nature* **408,** 453–457 (2000).
20. Webb, D. J. & Suginobara, N. Vertical mixing in the ocean. *Nature* **409,** 37 (2001).
21. Naveira Garabato, A. C., Heywood, K. J. & Stevens, D. P. Modification and pathways of Southern Ocean deep waters in the Scotia Sea. *Deep-Sea Res. I* (in the press).
22. Jackett, D. R. & McDougall, T. J. A neutral density variable for the world's oceans. *J. Phys. Oceanogr.* **27,** 237–263 (1997).
23. Naveira Garabato, A. C., McDonagh, E. L., Stevens, D. P., Heywood, K. J. & Sanders, R. J. On the export of Antarctic Bottom Water from the Weddell Sea. *Deep-Sea Res. II* (2002).
24. Arhan, M., Heywood, K. J. & King, B. A. The deep waters from the Southern Ocean at the entry to the Argentine Basin. *Deep-Sea Res. II* **46,** 475–499 (1999).
25. Orsi, A. H., Johnson, G. C. & Bullister, J. L. Circulation, mixing and production of Antarctic Bottom Water. *Prog. Oceanogr.* **43,** 55–109 (1999).
26. Egbert, G. D. & Ray, R. D. Significant dissipation of tidal energy in the deep ocean inferred from satellite altimeter data. *Nature* **405,** 775–778 (2000).
27. Sjoberg, B. & Stigebrandt, A. Computations of the geographical distribution of the energy flux to mixing processes via internal tide and the associated vertical circulation in the ocean. *Deep-Sea Res.* **39,** 269–291 (1992).
28. Bell, T. H. Topographically-generated internal waves in the open ocean. *J. Geophys. Res.* **80,** 320–327 (1975).
29. Fukumori, I., Raghunath, R. & Fu, L.-L. Nature of global large-scale sea level variability in relation to atmospheric forcing: a modelling study. *J. Geophys. Res.* **103,** 5493–5512 (1998).
30. Olbers, D., Gouretski, V., Seiss, G. & Schroter, J. *Hydrographic Atlas of the Southern Ocean* (Alfred Wegener Inst. for Polar and Marine Res., Bremerhaven, Germany, 1992).

Acknowledgements

We thank P. Barker and F. Vine for discussions regarding the magnitude of geothermal heating in the Scotia Sea. ALBATROSS was funded by the Natural Environment Research Council.

Competing interests statement

The authors declare that they have no competing financial interests.

Correspondence and requests for information should be addressed to K.J.H. (e-mail: k.heywood@uea.ac.uk).

Sudden aseismic fault slip on the south flank of Kilauea volcano

Peter Cervelli*†, Paul Segall*, Kaj Johnson*, Michael Lisowski‡ & Asta Miklius†

* *Department of Geophysics, Mitchell Building, Stanford University, Stanford, California 94305-2215, USA*
† *US Geological Survey, Hawaiian Volcano Observatory, Hawaii National Park, Hawaii 96718, USA*
‡ *US Geological Survey, Cascades Volcano Observatory, 5400 MacArthur Blvd, Vancouver, Washington 98661, USA*

One of the greatest hazards associated with oceanic volcanoes is not volcanic in nature, but lies with the potential for catastrophic flank failure[1,2]. Such flank failure can result in devastating tsunamis and threaten not only the immediate vicinity, but coastal cities along the entire rim of an ocean basin[3]. Kilauea volcano on the island of Hawaii, USA, is a potential source of such flank failures[3,4] and has therefore been monitored by a network of continuously recording geodetic instruments, including global positioning system (GPS) receivers, tilt meters and strain meters. Here we report that, in early November 2000, this network recorded transient southeastward displacements, which we interpret as an episode of aseismic fault slip. The duration of the event was about 36 hours, it had an equivalent moment magnitude of 5.7 and a maximum slip velocity of about 6 cm per day. Inversion of the GPS data reveals a shallow-dipping thrust fault at a depth of 4.5 km that we interpret as the down-dip extension of the Hilina Pali–Holei Pali normal fault system. This demonstrates that continuously recording geodetic networks can detect accelerating slip, potentially leading to warnings of volcanic flank collapse.

Data from the Kilauea GPS network (Fig. 1) are routinely analysed in 24-h batches at the US Geological Survey's Hawaiian Volcano Observatory (HVO). Figure 2 depicts the time series of selected stations on Kilauea's south flank as well as of three more distant stations. The south flank stations show clear offsets of up to 15 mm in early November, while the remote sites do not. The estimated displacements between 8 November and 10 November determined from the daily solutions are shown in Fig. 1. The spatial coherence of the signal and the negligible displacements far from the south flank (Fig. 1) rule out the possibility that the displacements are an artefact of unmodelled errors in the GPS time series.

We interpret the deformation field as resulting from fault slip. The data cannot be fitted by a dyke, sill, or expanding magma chamber. Moreover, there is no evidence of summit deflation, which usually accompanies magmatic activity. Nonlinear optimization[5] of the observed displacements for the best-fitting fault geometry yields a thrust, which dips shallowly ($4° \pm 10°$, uncertainties estimated using a bootstrap method[6]) toward the volcano (Figs 1 and 3). The average slip on the fault is 87 mm. The model-predicted displacements fit the observations, including the vertical components (Figs 1 and 3), extremely well (normalized mean square error of 1.2). The largest south flank earthquake during the first two weeks of November was a magnitude 2.7, which occurred on 3 November (Fig. 1). Thus, this event can be placed among the class of 'silent' earthquakes, which have been recently detected by large-scale

continuously recording geodetic networks[7,8]. This is, however, the first recording of a silent earthquake in a volcanic environment.

Many authors have suggested that the persistent seaward motion of Kilauea's south flank results from slip along a basal decollement[9–14] at a depth of 7–8 km (Fig. 3). The inferred depth of the November 2000 event, however, is too shallow for it to have occurred on this structure. Indeed, the uncertainties from the bootstrap analysis reject a decollement source at better than 95% confidence. Failure to account for material heterogeneity in the earth is thought to bias geodetic estimates of fault depth[15]. To address this concern, we used the best-fitting fault from the analysis above, which had assumed homogeneity, as a starting point for an inversion in a three-layer earth model. Green's functions for this model were computed using propagator matrices[16,17]. Rigidity was estimated from a seismic velocity model for Kilauea[18]. The estimated source depth does indeed increase, but only by 0.5 km. Assuming the variance of the depth estimated for the homogeneous model is a reasonable approximation to the actual variance, we can still rule out a decollement source with high confidence.

Other possible sources include listric normal faults associated with the Hilina Pali–Holei Pali fault system and shallow thrusts within the south flank wedge (Figs 1 and 3). Seismic reflection profiling[19] has imaged landward dipping reflectors that have been interpreted as thrust faults. Some of these structures have the same dip and approximate location as the modelled source of the November 2000 slip event (see, for example, Fig. 4 of ref. 19). Taken together, the normal faults and shallow thrusts are thought to comprise a large landslide structure. The data are consistent with the slip event having occurred on such a structure.

The daily GPS solutions put only broad constraints on the duration of the slip event. Conventional kinematic processing of the GPS data to produce solutions at shorter intervals should be capable of resolving a signal of 15 mm (refs 20, 21). However, the stations with the maximum displacements were offline during the slip event because of extensive flooding the previous week. Moreover, of the remaining stations, the one with the maximum displacement (KAEP) is situated in a high multipath environment, making sub-daily solutions poor. For these reasons, kinematic processing failed to demonstrate a convincing signal at individual stations.

Instead, we used the raw GPS observations to solve directly for fault slip as a function of time, as described in the Methods section. We find that slip began sometime after 18:00 on 8 November 2000 GMT and then proceeded at a nearly steady rate for about 36 hours (Fig. 4). Measurements from a borehole tilt meter (ESC, Fig. 1) and strain meter (STRS, Fig. 1) provide independent support for our estimate of the source duration. Figure 4 compares the observed tilt and strain to that predicted by the time-dependent slip model,

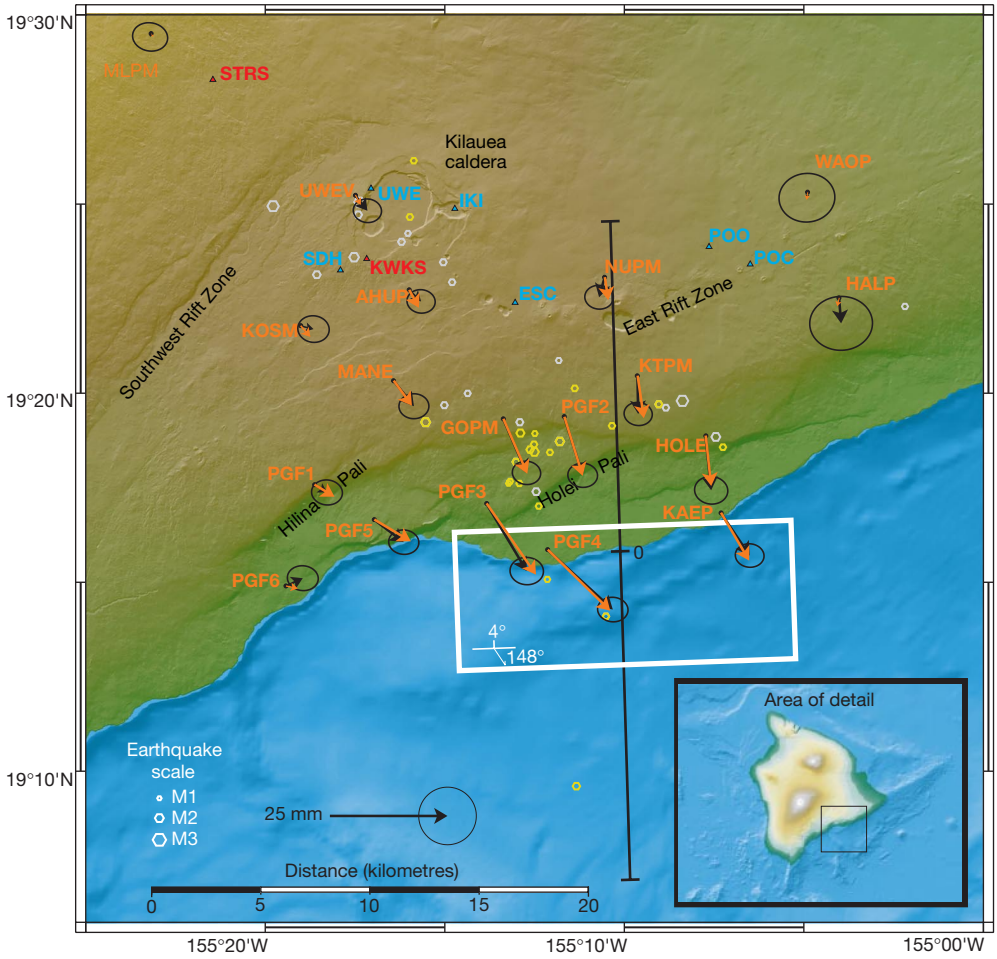

Figure 1 Observed (black) and predicted (orange) displacements from the November 2000 deformation event on Kilauea volcano. Error ellipses show 95% confidence regions, based on the scaled covariance of the GPS data (scaling was estimated from the day-to-day repeatability). Stations in white are continuous GPS; green stations are tilt meters; red stations are strain meters. Hexagons depict seismicity from 1 to 14 November 2000; those shown in yellow have source times within 36 h of the slip event. The white rectangle is the surface projection of the best-fitting source model (a uniform slip dislocation). The dimensions of the fault are 16 × 7 km; the total slip was 87 mm with a rake of 148°. These values and a nominal shear modulus of 3×10^{10} Pa lead to an equivalent seismic moment magnitude of M5.7. The black line locates the cross-section shown in Fig. 3. Inset, location of study area on the Big Island of Hawaii.

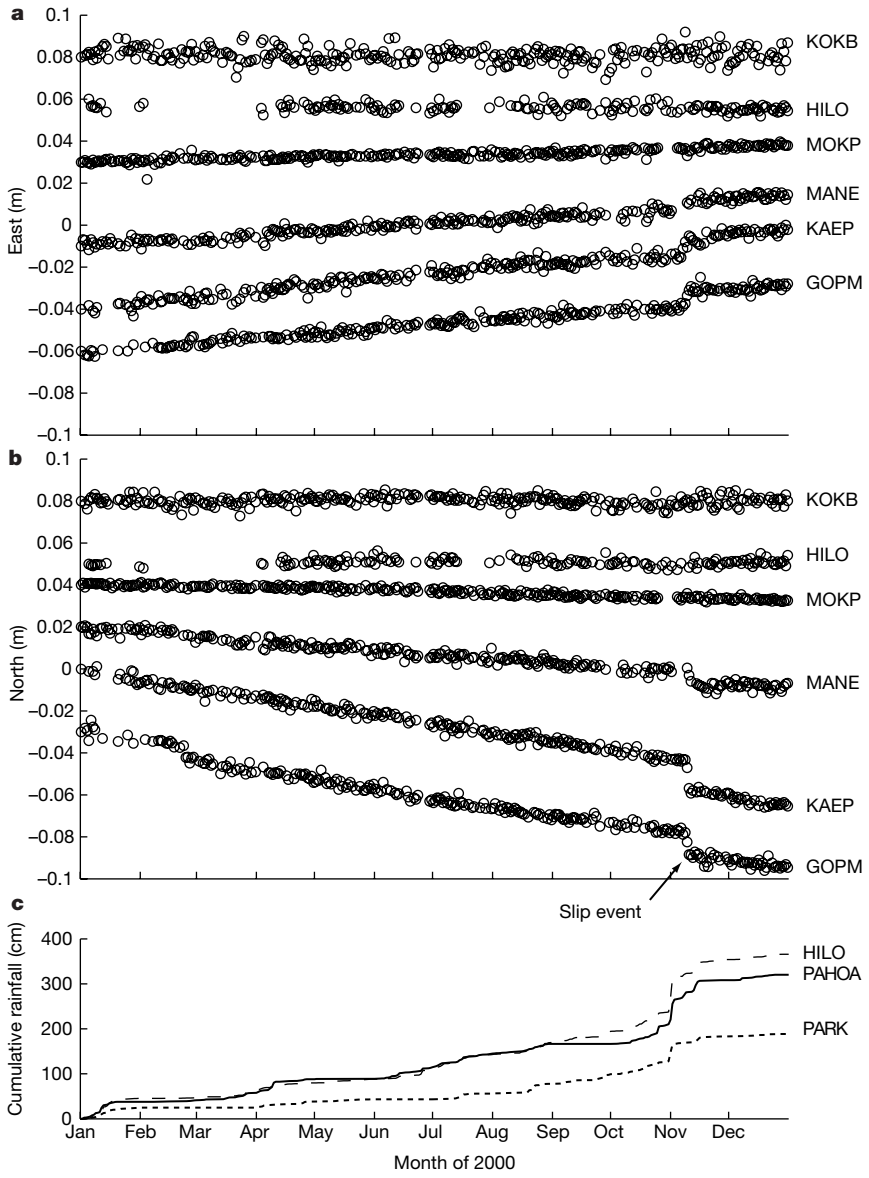

Figure 2 Horizontal displacement time series of six continuous GPS stations for 2000. The velocity of the station MKEA, near the summit of Mauna Kea, has been removed. **a**, **b**, The top three time series are from stations distant from Kilauea's south flank. KOKB is in Kokee Park, Kauai, HILO is at the airport in Hilo, Hawaii, and MOKP is on the summit of Mauna Loa volcano. **a**, **b**, The bottom three time series are from stations on the south flank (Fig. 1). Note the significant offsets that occur in the south-flank time series that do not occur at the more distant stations. **c**, Rainfall for the year 2000, measured at Hilo Airport, Pahoa School and Hawaii National Park Headquarters.

which was estimated using GPS data alone. Data from the remaining tilt and strain meters are substantially noisier, and although they are consistent with the model predictions, provide no additional information. The lack of a signal at the broad-band seismometer at Kipapa (on the Hawaiian island Oahu) is again consistent with the inferred source duration.

Nine days before the slip event, nearly 1 m of rain fell over the southeastern Big Island (Fig. 2). The timing of this storm suggests a possible causal relationship between the rainfall and the aseismic slip. Rainfall has two effects on fault stability. First, the surface loading instantaneously perturbs the stress throughout the south flank. Second, the elevated water table causes a pore pressure increase that diffuses into the volcano, decreasing the effective normal stress on faults and thereby bringing them closer to failure. The loading probably increased the Coulomb stress at the fault, but the magnitude of the change is a small fraction of the total surface load of approximately 0.1 MPa (for 1 m of water). The change in pore pressure induced at shallow depths is given by: $\Delta P = \rho g \Delta H/\phi$, where ρ is the density of water, g is the gravitational acceleration, ΔH is the change in water-table height and ϕ is porosity. A 1-m water-table change and a porosity of $\phi = 0.05$ increases pore pressures by 2 MPa, an amount capable of triggering fault slip[22]. For this pressure change to have triggered the slip, the fault-zone permeability must be sufficiently high for the pressure front to have reached the source region within the 10 days or so separating the rainfall and slip events. This requires a fault-zone diffusivity of $c = L^2/4t \approx 30\,\mathrm{m^2\,s^{-1}}$, where $L \approx 10^4$ m and $t \approx 10$ days. The corresponding permeability is given by $k = \eta\phi\beta c$, where η is the viscosity of water and β is a combination of pore and water compressibility. Using $\beta = 10^{-8}\,\mathrm{Pa^{-1}}$, a value for crack-like pores[23], we estimate an average permeability of $k \approx 10^{-10}\,\mathrm{m^2}$, which is consistent with permeability estimates[24] for highly fractured fault zones in Kilauea's south flank. A large fraction of the pressure change could have reached the source region if the permeability of the fault zone significantly exceeds that of the surrounding rock, preventing the pore pressure from dissipating into the

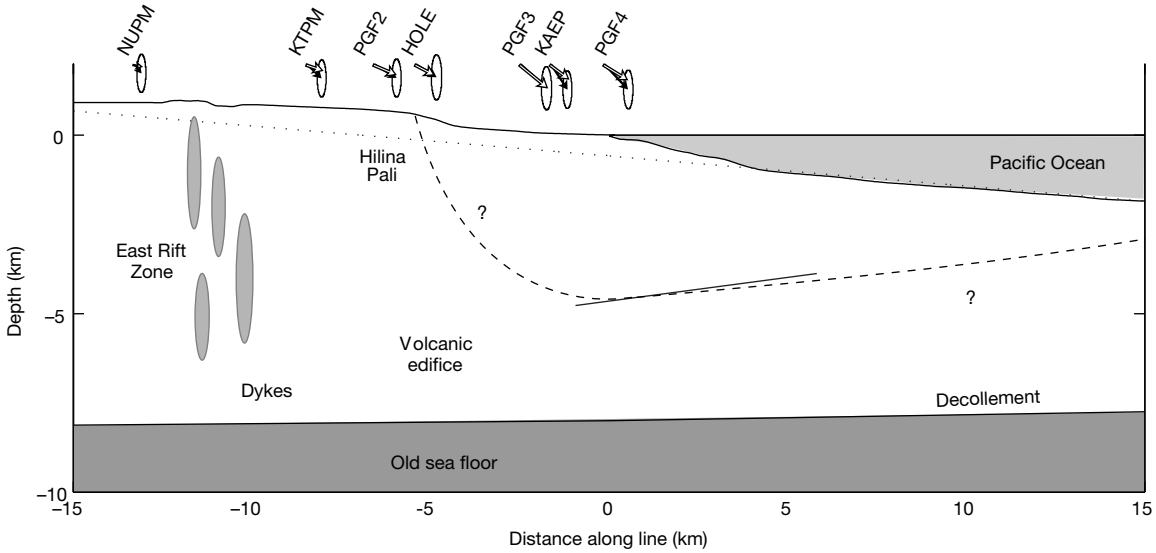

Figure 3 A cross-section of Kilauea's south flank along the grey line in Fig. 1. The geologic structure is inferred from seismic reflection data[19]. The location of the basal decollement is shown as a solid black line[11]. The dashed black line represents the top of the elastic body used as our earth model. This surface differs from the local horizontal because the elevation decreases monotonically to the southeast. In the source inversion, the dip and depth of the model fault are measured with respect to the top of the half-space. The model fault (solid line) lies near a region of thrust faults inferred from seismic reflection data[19], and may connect with the Hilina Pali–Holei Pali normal fault system (dashed). The cross-sectional area of the wedge above the fault system is about 50 km^2; extending the wedge 20 km in each direction along the strike give a potential slide volume of about 2,000 km^3, in the event of total disaggregation and failure.

volcano. Given the 10^{-15} m^2 permeability typical of the ash layers and the gabbroic rifts that surround the fault zone, this condition may have been met, although permeabilities at depth are highly uncertain.

From a geological perspective, the style and location of deformation from this event supports the view that the large normal faults cutting Kilauea's south flank are relatively shallow features that do not root into the decollement[25–27]. From a hazards perspective, flank failure on oceanic volcanoes represents an uncommon but significant danger to coastal cities. As these flanks begin to fail, they must accelerate. If slow acceleration precedes catastrophic failure, we have demonstrated that a well-placed geodetic network can detect such an acceleration, even when the absolute rates are small. The rate of slip observed in early November 2000 was about 5 cm per day, far faster than the slip rates (decimetres per year) inferred for Kilauea's decollement, but substantially less than catastrophic failure. For this slip event, the detection was after the fact, but there is no reason why the geodetic data could not be analysed in real time to provide a warning of sudden acceleration and potential flank instability. □

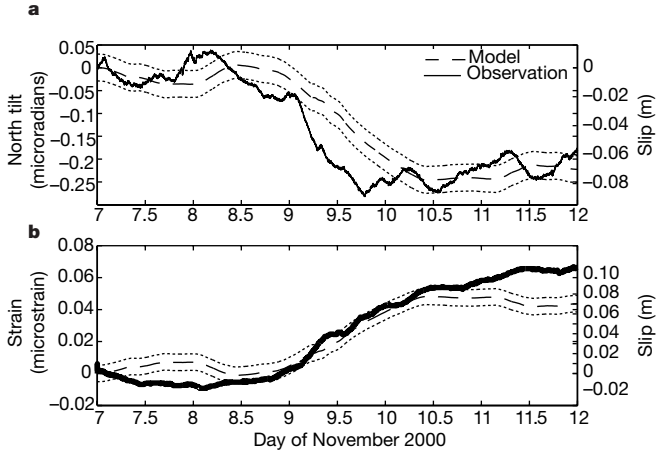

Figure 4 The source time function for November 2000 deformation event. **a**, The magnitude of the slip on the model fault (right scale, dashed line) and 95% uncertainty regions (dotted line), the predicted north tilt at station ESC (left scale, dashed line) and the observed north tilt at ESC (left scale, solid line), all as functions of time. **b**, Slip magnitude (right scale, dashed line) and 95% uncertainty regions (dotted line), predicted horizontal volumetric strain at STRS (left scale, dashed line) and observed volumetric strain at STRS (left scale, solid line). The apparent time lag between the observed and predicted tilt may be due either to the simplicity of the model (that is, the source geometry was fixed and slip was uniform) or to correlated errors in the tilt record. We varied the scale of the random walk process, σ_s, by a factor of 4 in each direction and found that the estimated duration of the event did not change significantly.

Methods

Estimating net displacements

We estimated the net displacements of the slip event from the daily GPS solutions, which are processed at HVO with the Gipsy/Oasis II software package[28] (http://gipsy.jpl.nasa.gov). We use a Kalman filter to model time variation of the station positions as the sum of the nominal station position, the long-term station velocity multiplied by the time, and a linearized Helmert transformation multiplied by a vector of reference frame parameters. This reduces the effect of reference frame uncertainty and allows empirical scaling of the GPS data covariance to a realistic value. The frame terms are assumed to be uncorrelated in time. The variance of the nominal station position term is reset to a large value at several specific epochs that correspond to dyke intrusions and earthquakes. This allows geologic offsets to exist in the time series without biasing the frame and the long-term velocity estimates.

Estimating the source time function

We used the raw GPS observations, which are sampled every 30 s, to solve directly for fault slip using the homogeneous elastic Green's functions from the best-fitting fault. This takes advantage of the spatial coherence of the deformation signal in the GPS network, effectively increasing the signal-to-noise ratio in the estimation of the temporal evolution of the source. Specifically, we model the double-differenced ionosphere-free carrier phase[29], $\Phi(t)$ (with wavelength λ) as:

$$\Phi(t) - r_0 = A\delta\boldsymbol{x}(t) + z(t)m_w + \lambda N \quad (1)$$

where r_0 are the predicted double-differenced ranges from the stations to the satellites, A is a matrix of partial derivatives of the double-difference ranges with respect to station coordinates, $\delta\boldsymbol{x}$ is a vector of time-varying differences in station coordinates from their nominal values, z is the time-varying tropospheric zenith delay, m_w is a tropospheric mapping function and N are the sums of the scaled integer phase ambiguities at the two GPS frequencies. The phase ambiguities suffer occasional cycle slips, which we detect and

flag in advance; N is reset when such slips occur. The double-differenced pseudoranges are modelled in the same way, with the exception of the phase ambiguity term, which is not needed. Instead of solving for $\delta \boldsymbol{x}$ for all the stations independently, we solve for a single slip parameter $s(t)$, such that $\delta \boldsymbol{x}(t) = Gs(t)$, where G are elastic functions relating slip on the model fault to displacement. We allow the slip to vary as a random walk in time, with scale σ_s. A nominal value of $\sigma_s = 3\,\mathrm{mm\,day^{-1/2}}$ is small enough to limit the scatter during periods without anomalous deformation, but large enough to allow the full 87 mm of slip to accumulate over approximately 24 hours. The time-dependent model fits the GPS double-difference phases to within 4 mm (root mean square).

Received 30 August 2001; accepted 21 January 2002.

1. McGuire, W. J. in *Volcano Instability on the Earth and Other Planets* (eds McGuire, W. J., Jones, A. P. & Neuberg, J.) 1–23 (Geological Society Spec. Publ. No. 110, London, 1996).
2. Moore, J. G. *et al.* Prodigious submarine landslides on the Hawaiian Ridge. *J. Geophys. Res.* **94,** 17465–17484 (1989).
3. Ward, S. Landslide tsunami. *J. Geophys. Res.* **106,** 11201–11216 (2001).
4. Lipman, P. W., Normark, W. R., Moore, J. G., Wilson, J. B. & Gutmacher, C. E. The giant submarine Alika debris slide, Mauna Loa, Hawaii. *J. Geophys. Res.* **94,** 4279–4299 (1988).
5. Cervelli, P., Murray, M. H., Segall, P., Aoki, Y. & Kato, T. Estimating source parameters from deformation data, with an application to the March 1997 earthquake swarm off the Izu Peninsula, Japan. *J. Geophys. Res.* **106,** 11217–11238 (2001).
6. Efron, B. & Tibshirani, R. J. *An Introduction to the Bootstrap* (Chapman and Hall, New York, 1993).
7. Linde, A. T., Gladwin, M. T., Johnston, M. J. S., Gwyther, R. L. & Bilham, R. G. A slow earthquake sequence on the San Andreas fault. *Nature* **383,** 65–68 (1996).
8. Dragert, H., Wang, K. & James, T. S. A silent slip event on the deeper Cascadia subduction interface. *Science* **292,** 1525–1528 (2001).
9. Nakamura, K. Why do long rift zones develop in Hawaiian volcanoes—A possible role of thick oceanic sediments. *Bull. Volcanol. Soc. Jpn* **25,** 255–267 (1980) (in Japanese).
10. Dieterich, J. H. Growth and persistence of Hawaiian rift zones. *J. Geophys. Res.* **93,** 4258–4270 (1988).
11. Thurber, C. H. & Gripp, A. E. Flexure and seismicity beneath the south flank of Kilauea Volcano and tectonic implications. *J. Geophys. Res.* **93,** 4271–4278 (1988).
12. Delaney, P. T., Miklius, A., Árnadóttir, T., Okamura, A. T. & Sako, M. K. Motion of Kilauea Volcano during sustained eruption from the Pu'u O'o and Kupaianaha vents, 1983–1991. *J. Geophys. Res.* **98,** 17801–17820 (1993).
13. Owen, S. *et al.* Rapid deformation of the south flank of Kilauea Volcano, Hawaii. *Science* **267,** 1328–1332 (1995).
14. Owen, S. *et al.* Rapid deformation of Kilauea volcano: GPS measurements between 1990 and 1996. *J. Geophys. Res.* **105,** 18983–18998 (2000).
15. Du, Y., Segall, P. & Gao, H. Quasi-static dislocations in three dimensional inhomogeneous media. *Geophys. Res. Lett.* **24,** 2347–2350 (1997).
16. Aki, K. & Richards, P. G. *Quantitative Seismology; Theory and Methods* (Freeman, San Francisco, 1970).
17. Ward, S. N. Quasi-static propagator matrices: creep on strike-slip faults. *Tectonophysics* **120,** 83–106 (1985).
18. Okubo, P. G., Benz, H. M. & Chouet, B. A. Imaging the crustal magma sources beneath Mauna Loa and Kilauea volcanoes, Hawaii. *Geology* **25,** 867–870 (1997).
19. Morgan, J. K., Moore, G. F., Hills, D. J. & Leslie, S. Overthrusting and sediment accretion along Kilauea's mobile south flank, Hawaii: Evidence for volcanic spreading from marine seismic reflection data. *Geology* **28,** 667–670 (2000).
20. Elosegui, P., Davis, J., Johansson, J. & Shapiro, I. Detection of transient motions with the Global Positioning System. *J. Geophys. Res.* **101,** 11249–11261 (1996).
21. Larson, K. *et al.* Volcano monitoring using kinematic GPS: Filtering strategies. *J. Geophys. Res.* **106,** 19453–19464 (2001).
22. Stein, R. S. The role of stress transfer in earthquake occurrence. *Nature* **402,** 605–609 (1999).
23. David, C., Wong, T.-F., Zhu, W. & Zhang, J. Laboratory measurements of compaction-induced permeability change in porous rocks; implications for the generation and maintenance of pore pressure excess in the crust. *Pure Appl. Geophys.* **143,** 425–456 (1994).
24. Ingebritsen, S. E. & Scholl, M. A. The hydrology of Kilauea Volcano. *Geothermics* **22,** 255–270 (1993).
25. Swanson, D. A., Duffield, W. A. & Fiske, R. S. Displacement of the south flank of Kilauea Volcano: The result of forceful intrusion of magma into the rift zones. *US Geol. Surv. Prof. Pap.* **963,** 1–30 (1976).
26. Dvorak, J. J., Klein, F. W. & Swanson, D. A. Relaxation of the south flank after the 7.2-Magnitude Kalapana earthquake, Kilauea volcano, Hawaii. *Bull. Seismol. Soc. Am.* **84,** 133–141 (1994).
27. Cannon, E. C., Bürgmann, R. & Owen, S. E. Shallow normal faulting and block rotation associated with the 1975 Kalapana earthquake, Kilauea Volcano, Hawaii. *Bull. Seismol. Soc. Am.* (in the press).
28. Lichten, S. & Borden, J. Strategies for high-precision Global Positioning System orbit determination. *J. Geophys. Res.* **92,** 12751–12762 (1987).
29. Hofmann-Wellenhof, B., Lichtenegger, H. & Collins, J. *GPS: Theory and Practice* (Springer, New York, 1994).

Acknowledgements

We thank M. Bevis for access to the GPS data for the University of Hawaii network, P. Okubo for providing hypocentres, G. Blewitt, R. Bürgmann, J. Davis, R. Iverson, M. Johnston, J. McGuire, J. Murray, D. Swanson and W. Thatcher for comments and discussion, and D. Okita for getting us to and from Kilauea GPS stations safely and efficiently. The National Science Foundation and the US Geological Survey provided funding for this research.

Competing interests statement

The authors declare that they have no competing financial interests.

Correspondence and requests for materials should be addressed to P.C. (e-mail: cervelli@sumo.wr.usgs.gov).

Tyrannosaurus was not a fast runner

John R. Hutchinson*† & Mariano Garcia*†

* *Department of Integrative Biology, University of California, Berkeley, California 94720-3140, USA*
† *Present addresses: Biomechanical Engineering Division, Stanford University, Stanford, California 94305-4038, USA (J.R.H.); Borg-Warner Automotive, 770 Warren Road, Ithaca, New York 14850, USA (M.G.)*

The fastest gait and speed of the largest theropod (carnivorous) dinosaurs, such as *Tyrannosaurus*, is controversial. Some studies contend that *Tyrannosaurus* was limited to walking, or at best an 11 m s^{-1} top speed[1–4], whereas others argue for at least 20 m s^{-1} running speeds[5–7]. We demonstrate a method of gauging running ability by estimating the minimum mass of extensor (supportive) muscle needed for fast running. The model's predictions are validated for living alligators and chickens. Applying the method to small dinosaurs corroborates other studies by showing that they could have been competent runners. However, models show that in order to run quickly, an adult *Tyrannosaurus* would have needed an unreasonably large mass of extensor muscle, even with generous assumptions. Therefore, it is doubtful that *Tyrannosaurus* and other huge dinosaurs (~6,000 kg) were capable runners or could reach high speeds.

Most assessments of running ability in large theropods are qualitative, based on analogies to walking elephants or running birds and hoofed mammals[3,5–7]. Earlier quantitative assessments of the biomechanics of *Tyrannosaurus* suggested that it had limited locomotor performance[1,2,4,8,9], but uncertainties about tyrannosaur anatomy, physiology, and behaviour have impeded resolution of this debate[1–9]. Fossilized footprints demonstrate that smaller theropod dinosaurs could run[10], but running tracks from large theropods are unknown[7,9]. Bulky limbs and other analogies with elephants

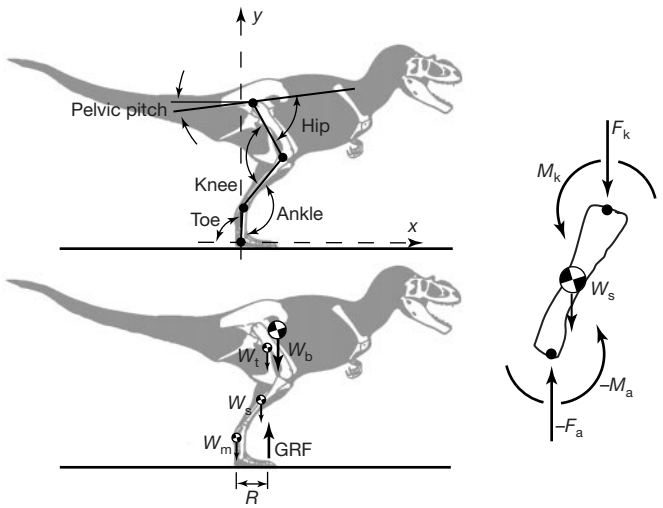

Figure 1 Explanation of free-body diagram analysis of body segments. Skeletal illustration modified from ref. 6. The initial *Tyrannosaurus* model (Trex_1) is shown in right lateral view and (x, y)-coordinate space, with the origin located at the toe joint. Pelvic pitch, hip, knee, ankle and toe joint angle definitions are shown (see Supplementary Information). One of the angles is redundant (four angles suffice). The ground reaction force (GRF) is vertical (typical for mid-stance[12–14]) and acts at a distance R from the toe joints. The body segment weights (W_b, W_t, W_s and W_m for the trunk, thigh, shank and metatarsus) are also shown. A free-body diagram was used to calculate the internal moments about each joint. For example, about the knee joint (see inset), the moment that knee extensor muscles must generate (M_k) is equal to the ankle contact force ($-F_a$) times its respective moment arm, plus the gravitational moment of the shank segment and the ankle moment ($-M_a$).